8B.3

Moving Quasigeostrophic Theory into the 21st Century

Eric R. Thaler[1]
NOAA/National Weather Service, Denver/Boulder, Colorado

Paul Nutter
Earth Sciences Program, University of Northern Colorado, Greeley, Colorado

Introduction

Quasigeostrophic (QG) theory has been a central part of synoptic scale meteorology for well over half a century. It was used quantitatively in the early days of numerical weather prediction and has been applied qualitatively for decades, in one form or another, in operational weather forecasting and research in synoptic scale dynamics. Moreover, QG theory is a staple in nearly all, if not all, dynamic meteorology courses at both the undergraduate and graduate level.

Unfortunately, most applications of QG theory in operational forecasting, research studies and meteorological education has changed little during this time. One notable exception is the use of Q-vectors to diagnose vertical motions via the omega equation rather than evaluating the forcing associated with temperature and vorticity advection. However, the implementation of high resolution numerical analyses and forecasts has made both of these older application methods difficult, if not impossible, to implement.

The increase in computing power that has produced these high resolution data sets has also led to the capability of applying QG theory using more robust quantitative procedures. This has been manifest at the National Weather Service Forecast Office in Denver/Boulder through the use of a complete QG analysis package that goes well beyond the typical applications of the theory. The package provides full three dimensional numerical solutions to the QG omega, height tendency and Zwack-Okossi development equations. In addition, a variety of other QG related fields are computed including deformation, static stability tendency, frontogenesis, and others. The package allows forecasters to easily diagnose the synoptic scale dynamics both in the analyses and forecasts. Furthermore, although not yet implemented, the package could easily be used in the classroom to revolutionize the way meteorology students are introduced to QG theory by avoiding the relatively large number of assumptions, some of which are rather questionable, that are usually considered to make the presentation more tractable.

This paper will discuss some of the features of this package, share a few insights that have been gained through its operational use, and perhaps suggest ways that the package could be used in the classroom.

Data and computational procedures

The QG package is run locally, in real time, at the Weather Forecast Office in Denver/Boulder on a Linux workstation. A wide variety of diagnostic fields are produced, allowing forecasters (and potentially students in synoptic/dynamic meteorology courses) to obtain a rather complete QG picture of the atmosphere. The novel approach here is to not only provide the "usual" fields typically used in synoptic/dynamic diagnosis (temperature advection, differential vorticity advection, divergence of Q-vectors, *etc.*) but to also produce solutions of the fundamental diagnostic equations of QG theory. These equations are show in the Appendix; mathematical variables follow standard meteorological conventions.

The diagnostic parameters and numerical solutions to the aforementioned equations are computed using all of the numerical weather prediction (NWP) data received at National Weather Service offices. This includes the North American Mesoscale (NAM), Global Forecast System (GFS), Rapid Update Cycle (RUC), United Kingdom Meteorological Office (UKMET), European Centre for Medium-Range Weather Forecasts (ECMWF), and Downscaled GFS by NAM extension (DGEX). In addition, the equations are solved using the mean fields from the Short Range Ensemble Forecast (SREF) and Global Ensemble Forecast System. Solutions using data from Environment Canada's Global Environmental Multiscale

[1] *Corresponding author address*: Dr. Eric Thaler, National Weather Service, WS1, 325 Broadway, Boulder, Colorado 80305; E-mail: eric.thaler@noaa.gov

(GEM) model will be coming on line in the near future.

An outline of the solution technique is as follows. Further details can be found in Thaler (2004). Height fields and surface pressure are extracted from the raw model data and, if not already there, placed on the CONUS211 grid, which has a nominal horizontal grid point spacing of 80 km. For higher resolution data sets, this remapping to the CONUS211 grid requires the data to be thinned (by using a subset of all the grid points), while lower resolution data is bilinearly interpolated to the smaller grid. Once the height fields are remapped, if necessary, they are vertically interpolated to a 50 hPa grid extending from 1000 hPa to 100 hPa. The height and surface pressure fields are then smoothed using an implicit tangent filter (Raymond, 1988) to eliminate smaller scale features. At this point, vertical height gradients are computed from these smoothed height fields using a fourth order compact operator scheme for the derivatives with virtual temperatures then calculated from these gradients using the hydrostatic equation. The static stability as well as the remaining forcing terms (those on the right hand side) in the QG omega equation [Eq. (1)] are then calculated. In order for Eqs. (1) and (2) to be elliptic partial differential equations the static stability must be positive definite, so a check is made to ensure that this is the case. Numerical solution of Eq. (1) requires the specification of boundary conditions. Homogeneous Dirichlet boundary conditions ($\omega = 0$) are used at the top of the domain and on the lateral boundaries. A linearized nonhomogeneous Dirichlet boundary condition is applied on the bottom boundary (1000 hPa), which essentially assumes that the surface geostrophic wind flows over the terrain. The QG omega equation [Eq. (1)] is then numerically solved using the preconditioned, stabilized bi-conjugate gradient method.This iterative technique is substantially faster than the successive over-relaxation (SOR) method that is usually implemented to solve the QG omega equation, requiring on the order of 50 iterations to converge to a solution compared to several hundred required for SOR. Next, the right hand side of the Zwack-Okossi development equation [Eq. (3)] is calculated, using the values for ω obtained above. The same iterative technique discussed previously is used to invert the Laplacian in Eq. (3) to yield $\frac{\partial \Phi(p_l)}{\partial t}$, the geopotential (height) tendency at the "surface", defined as the first grid point where the pressure is less than the terrain pressure. Homogeneous Dirichlet lateral boundary conditions are used during the inversion. This field then serves as the nonhomogeneous Dirichlet lower boundary condition during the solution of the geopotential tendency equation [Eq. (2)]. Homogeneous Dirichlet conditions are specified on the top and lateral boundaries during the iterative solution of this equation. The final step in the calculations is the computation of a QG "precipitation rate", computed by lifting the model moisture field with the newly computed QG vertical velocity. All of the output from the QG package is then available for real time use in daily forecast operations. The data can be trivially combined with all other data currently available to forecasters (*e.g.*, satellite, radar, upper air, *etc.*)

It should be emphasized here that the solution technique contains some subtleties that have, for the most part, been ignored previously. These include the use of a crude large scale terrain forcing via the nonhomogeneous lower boundary conditions, fully three-dimensionally varying static stability parameter, inclusion of moisture via virtual temperature and the inclusion of the beta effect. These variations from the traditional solution techniques can have profound effects on the standard interpretations of the diagnostic equations as given, for example, in Holton (1992) and Bluestein (1993).

Discussion

One can make the argument that the use of QG theory in this age of high resolution data sets and numerical weather prediction models is outdated. Perhaps forecasters (and students) should just use the NWP output verbatim without trying to understand the underlying dynamics. Indeed, there is anecdotal evidence suggesting that "meteorological cancer" discussed nearly three decades ago by Snellman (1982) and more recently by Bosart (2003) is becoming increasingly prominent in the operational meteorological community. While QG theory certainly cannot explain all weather phenomena, when applied properly (namely by way of actual solutions to the diagnostic equations rather than relying on questionable assumption-laden approximations) it is capable of explaining a rather wide range of weather conditions, even those where the assumptions underlying the theory could be called into question. Furthermore, viewing the atmosphere through the QG filter also allows one to better differentiate between synoptic scale and mesoscale or smaller phenomena.

As a first example of the benefits of using the QG

diagnostic package, consider Fig. 1, which shows numerical model output of heights and vertical motion. The vertical velocity field is extremely noisy, containing a large number of small scale features, some related to the synoptic scale troughs and ridges, others due to the underlying terrain and still others likely due to gravity waves in the model. When confronted with data like this, it is not a simple matter to understand the causes of all the vertical motion features shown. If the forecaster is attempting to understand the development of precipitation using the model vertical motion, it is often not clear as to which came first, the precipitation creating the vertical motion due to latent heat effects or the vertical motion leading to the creation of precipitation at a later time through saturated ascent. Sorting all of this out when facing operational deadlines is difficult.

Contrast this with Fig. 2, depicting the height field and radar reflectivity along with the QG vertical velocity [solution of Eq. (1)] for the same time as in Fig. 1. The comma shaped area of ascent lines up nicely with the similarly shaped radar echoes, with the strong subsidence normally found on the upstream side of a synoptic scale trough clearly visible near the center of the figure. The other area of precipitation over the Great Basin is also in an area of QG ascent associated with another synoptic scale trough. It appears that much of the precipitation depicted seems to be forced by QG processes. The notable exception to this would be the precipitation along the West Coast, which appears in QG subsidence areas but is probably forced by terrain.

The next example of the usefulness of the QG diagnostic package is shown in Fig. 3. Here is a rather innocuous trough in the height field along with the QG vertical velocity. It is interesting to note that the usual conceptual model of ascent ahead of the trough axis and subsidence behind fails to work properly here, with a substantial area of ascent/descent shown behind/ahead of the trough axis, likely due to frontogenetical processes associated with the confluent flow to the southeast of the trough. Again, having the actual QG vertical velocity at their disposal, forecasters can easily see these kinds of departures from the standard conceptual models. Moreover, giving meteorology students access to such depictions early in their careers would likely prove beneficial too as they may not fall into the trap of trying to fit all flow patterns into cookie-cutter like compartments.

The standard textbook approach of discussing the QG diagnostic equations and their solutions involves the approximation that the solution of the equations is negatively correlated with the forcing functions. This requires some questionable "hand-waving" type of mathematical arguments. That this is not necessarily always true is shown in Fig. 4 where the forcing function and the solution to the geopotential tendency equation [Eq. (2)] are shown together. It is obvious from this depiction that the maxima/minima of the forcing function are not necessarily correlated (either negatively or positively) with the maxima/minima of the solution to the equation. While these types of mathematical simplifications may provide some physical insights into the equations, one wonders if they do more harm than good. Assuming that a three dimensional Laplace operator behaves as simply as a sign change can lead to significant misinterpretations of the diagnostic equations. It also leads to questions about the applicability of the equations to real weather scenarios.

Figure (5) shows an example of the QG precipitation rate discussed above, combined with radar imagery. Although not perfect, the ability of QG theory to capture at least the gross features of the rain band is striking. It is also an interesting exercise to complete a more thorough QG analysis of this band of ongoing precipitation. To begin, Fig. 6 shows the virtual temperature, geostrophic wind, dilatation axes of the geostrophic deformation (aligned along the local axis of dilatation) and geostrophic frontogenesis function at the time of the rain band. Most of the area in the figure is experiencing geostrophic frontogenesis with a small area of frontolysis shown near the center (dashed lines). This frontogenesis is a quantitative depiction of the action of the geostrophic deformation acting on the virtual temperature gradient (Petterssen, 1956). Figure 7 takes this a step further by showing the relative humidity field, the forcing function in the omega equation due to the frontogenesis and the actual QG vertical motion response forced by the frontogenesis. The ascending branch of the direct circulation is plainly visible and when this is combined with the relative humidity field it becomes clear that this band is likely forced in large part by QG processes. Note also that the actual solution to the omega equation is substantially smoother than the forcing function. Indeed the response to the frontolytical area is completely absent in the actual vertical motion solution. This provides more reason to use the solutions to the diagnostic equations rather than the forcing functions as the interpretation is much simpler. Many of the small scale forcing function fea-

tures in the equations simply do not have an impact on the solutions. Trying to estimate the solution to the equations by putting all of these pieces together, either from a student's perspective or a forecaster's, is nontrivial.

Finally, an example of the solution to the Zwack-Okossi development equation [Eq. (3)] is shown in Fig. 8. This equation essentially integrates all QG processes throughout the atmosphere to obtain a pressure tendency at the surface. This parameter is helpful in understanding the movement and intensification or decay of low level pressure systems. It is also helpful in discerning when ageostrophic processes are dominant.

Concluding remarks

This paper has briefly described a QG diagnostic package that has been in use at the NWS office in Denver/Boulder, Colorado for the last several years. It has proven to be quite beneficial to the forecast process by allowing forecasters to gain a deeper understanding of large scale processes both in the actual atmosphere and in the numerical weather prediction model output. It has also been briefly discussed in some classroom settings up to this point, but not yet implemented there. However, it is felt that having a package like this available in the classroom could also prove useful in teaching both undergraduate and graduate students synoptic and dynamic meteorology.

Acknowledgments

Python programming assistance from Tom Lefebvre at ESRL/GSD is gratefully acknowledged. The willingness of the forecast staff at WFO Denver/Boulder to integrate new data sets into their daily operations is also much appreciated.

References

Bluestein, H., 1993: *Synoptic/Dynamic Meteorology in Midlatitudes Volume I: Principles of Kinematics and Dynamics*. Oxford University Press, 431 pp.

Bosart, L. F., 2003: Whither the weather analysis and forecasting process? *Wea. Forecasting*, **18(3)**, 520–529.

Holton, J., 1992: *Introduction to Dynamic Meteorology*. Third ed., Academic Press, 507 pp.

Petterssen, S., 1956: *Weather Analysis and Forecasting Volume I: Motion and Motion Systems*. Second ed., McGraw-Hill Book Company, Inc., 428 pp.

Raymond, W. H., 1988: High-order low-pass implicit tangent filters for use in finite area calculations. *Mon. Wea. Rev.*, **116(11)**, 2132–2141.

Snellman, L. W., 1982: Impact of AFOS on operational forecasting. *Preprints 9th Conf. Wea. Anal. Forecasting*, Amer. Meteor. Soc., Seattle, WA, 13–16.

Thaler, E. R., 2004: An evaluation of the operational use of numerical solutions to the quasi-geostrophic diagnostic equations by weather forecasters. Ph.D. thesis, Department of Applied Mathematics, University of Colorado, 171 pp., [Available online at `http://amath.colorado.edu/activities/thesis/thaler/thesis.pdf`].

Appendix

Quasigeostrophic Omega Equation

$$\nabla_p^2\left[\frac{R_d}{p}\left(\frac{R_dT_v}{pc_{p_d}}-\frac{\partial T_v}{\partial p}\right)\omega\right]+f_o^2\frac{\partial^2\omega}{\partial p^2}=2\left\{\frac{\partial}{\partial x}\left[\frac{\partial u_g}{\partial x}\frac{\partial}{\partial x}\left(\frac{R_dT_v}{p}\right)+\frac{\partial v_g}{\partial x}\frac{\partial}{\partial y}\left(\frac{R_dT_v}{p}\right)\right]+\right.$$
$$\left.\frac{\partial}{\partial y}\left[\frac{\partial u_g}{\partial y}\frac{\partial}{\partial x}\left(\frac{R_dT_v}{p}\right)+\frac{\partial v_g}{\partial y}\frac{\partial}{\partial y}\left(\frac{R_dT_v}{p}\right)\right]\right\}-\beta\frac{\partial}{\partial x}\left(\frac{R_dT_v}{p}\right)-f_o\frac{\partial}{\partial p}\left(\frac{\partial F_{r_y}}{\partial x}-\frac{\partial F_{r_x}}{\partial y}\right)-\nabla_p^2\left(\frac{R_d\dot{H}}{pc_{p_d}}\right) \quad (1)$$

Quasigeostrophic Geopotential Tendency Equation

$$\left[\frac{R_d}{p}\left(\frac{R_dT_v}{pc_{p_d}}-\frac{\partial T_v}{\partial p}\right)\right]\nabla_p^2\frac{\partial\Phi}{\partial t}+f_0^2\frac{\partial^2}{\partial p^2}\frac{\partial\Phi}{\partial t}=-f_o\left[\frac{R_d}{p}\left(\frac{R_dT_v}{pc_{p_d}}-\frac{\partial T_v}{\partial p}\right)\right]\mathbf{V}_g\cdot\nabla_p\left(\zeta_g+f\right)$$
$$-f_o^2\frac{\partial}{\partial p}\left[-\mathbf{V}_g\cdot\nabla_p\left(\frac{R_dT_v}{p}\right)\right]-f_o^2\omega\frac{\partial}{\partial p}\left[\frac{R_d}{p}\left(\frac{R_dT_v}{pc_{p_d}}-\frac{\partial T_v}{\partial p}\right)\right]$$
$$+f_o\left[\frac{R_d}{p}\left(\frac{R_dT_v}{pc_{p_d}}-\frac{\partial T_v}{\partial p}\right)\right]\left(\frac{\partial F_{r_y}}{\partial x}-\frac{\partial F_{r_x}}{\partial y}\right)-f_o^2\frac{\partial}{\partial p}\left(\frac{R_d\dot{H}}{pc_{p_d}}\right) \quad (2)$$

Quasigeostrophic Zwack-Okossi Development Equation

$$\nabla_p^2\frac{\partial\Phi(p_l)}{\partial t}=\frac{1}{(p_t-p_l)}\int_{p_l}^{p_t}\left[-f_o\mathbf{V}_g\cdot\nabla_p\left(\zeta_g+f\right)+\left(\frac{\partial F_{r_y}}{\partial x}-\frac{\partial F_{r_x}}{\partial y}\right)\right]\mathrm{d}p+f_o^2\frac{\omega(p_t)-\omega(p_l)}{p_t-p_l}$$
$$+\frac{1}{p_t-p_l}\int_{p_l}^{p_t}\int_{p_l}^{p}\nabla_p^2\left[-\mathbf{V}_g\cdot\nabla_p\left(\frac{R_dT_v}{p^\star}\right)+\frac{R_d}{p^\star}\left(\frac{R_dT_v}{p^\star c_{p_d}}-\frac{\partial T_v}{\partial p}\right)\omega+\frac{R_d\dot{H}}{p^\star c_{p_d}}\right]\mathrm{d}p^\star\mathrm{d}p \quad (3)$$

Figures

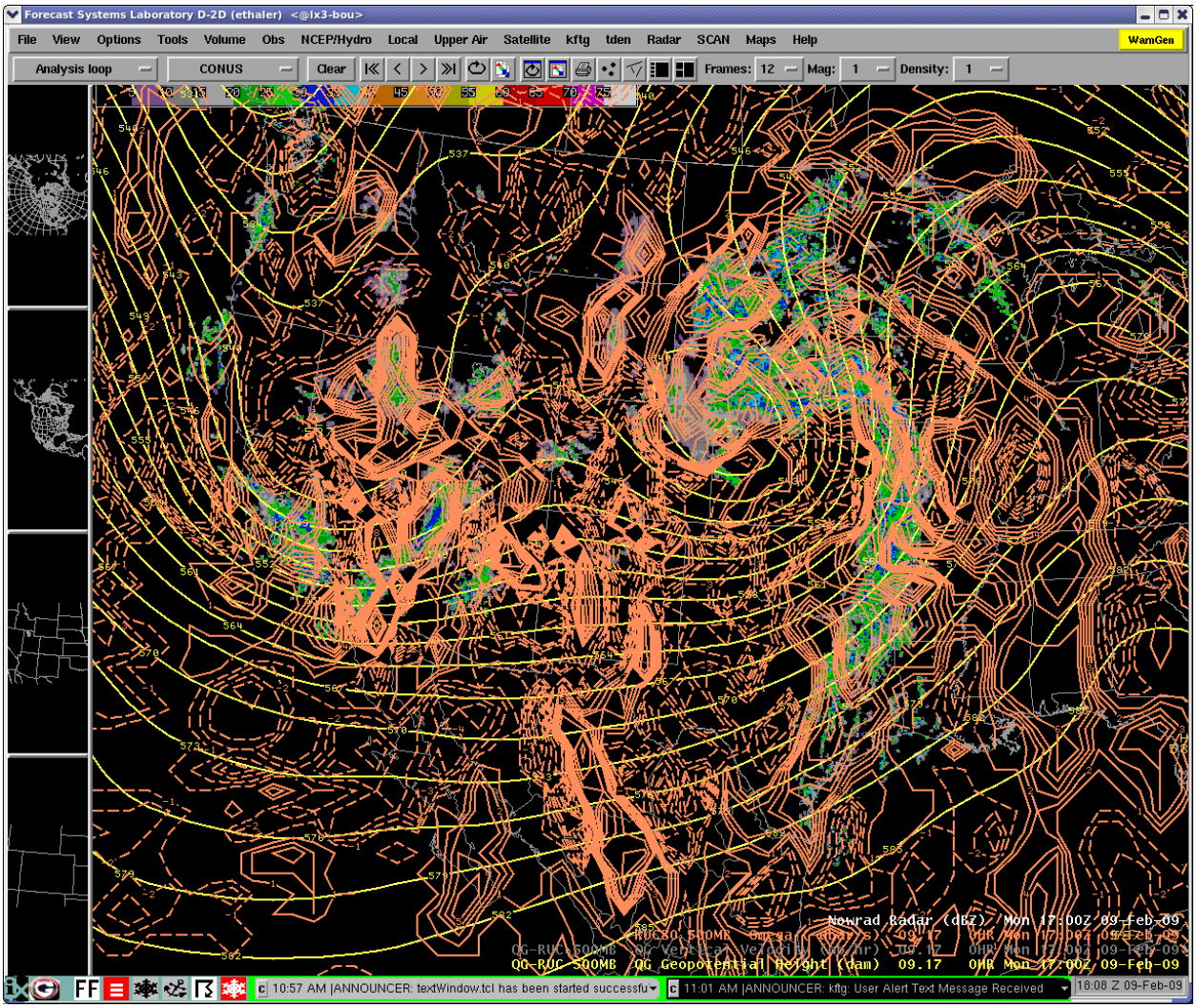

Figure 1: 500 hPa height (yellow, dam), primitive equation vertical velocity (orange, μbar s^{-1}, solid lines denote ascent, dashed lines descent) and radar reflectivity (dBZ, scale at top).

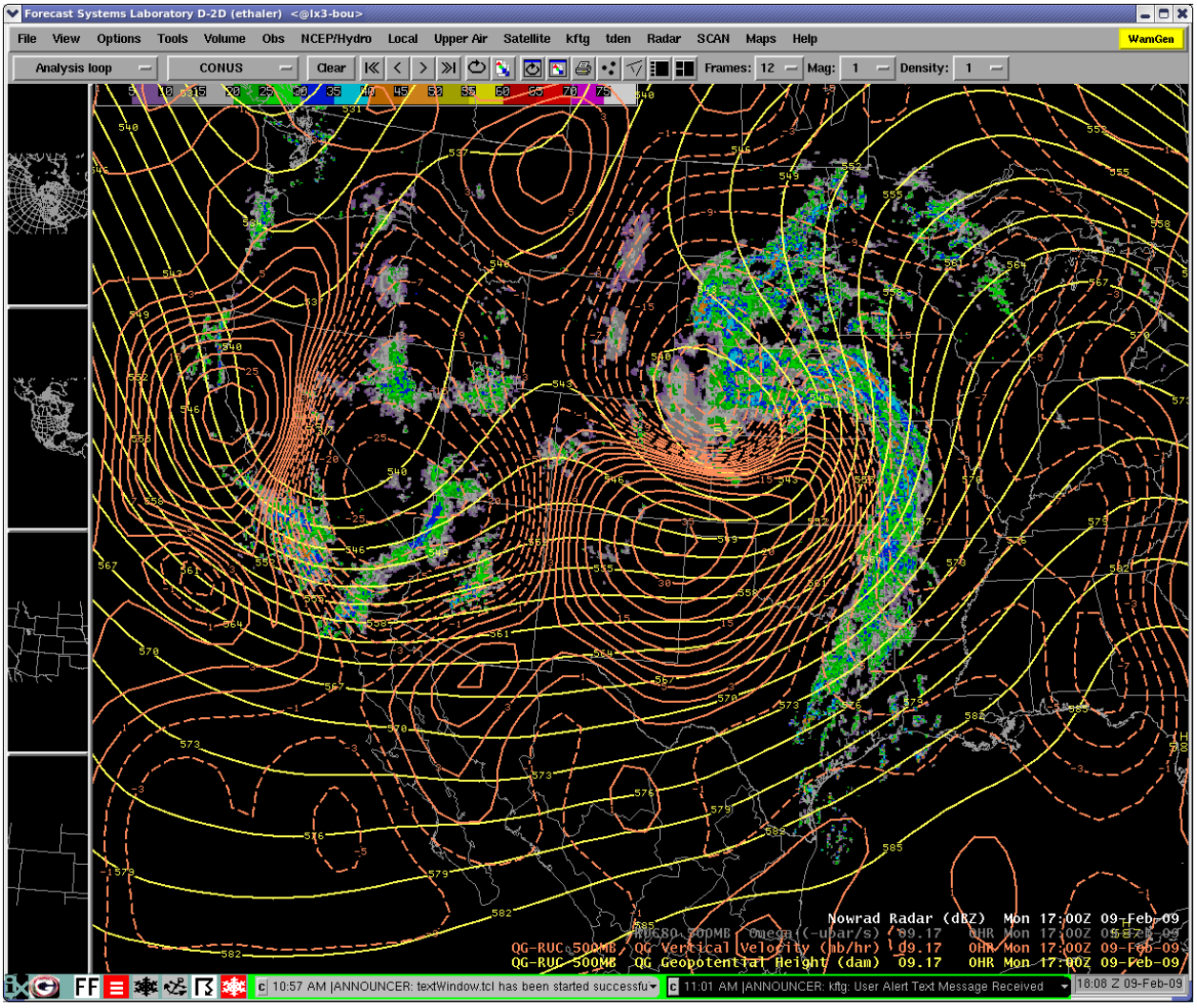

Figure 2: 500 hPa height (yellow, dam), QG vertical velocity (orange, hPa hr^{-1}, solid lines denote descent, dashed lines ascent) and radar reflectivity (dBZ, scale at top).

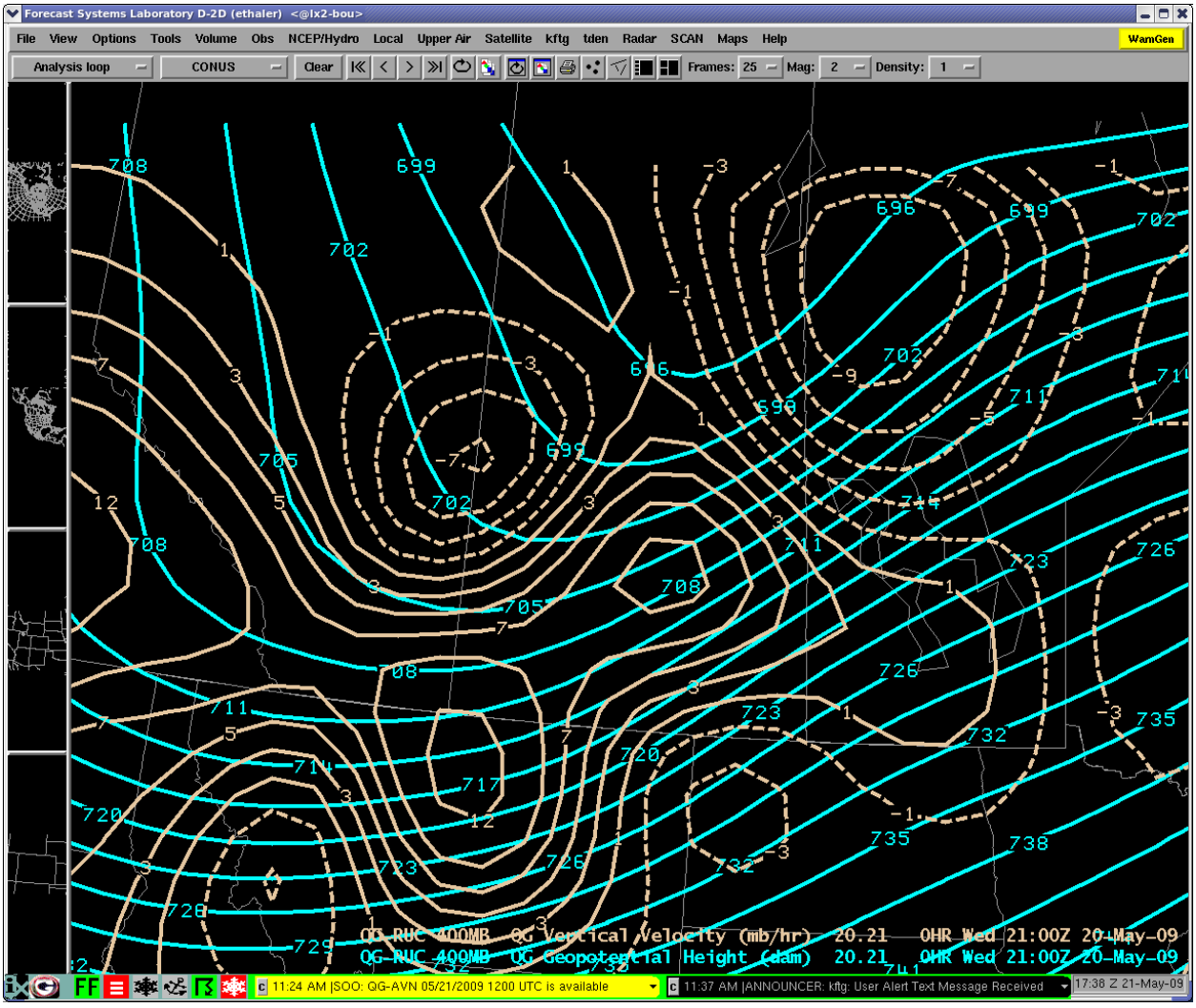

Figure 3: 400 hPa height (blue, dam) and QG vertical velocity (tan, hPa hr^{-1}, solid lines denote descent, dashed lines ascent).

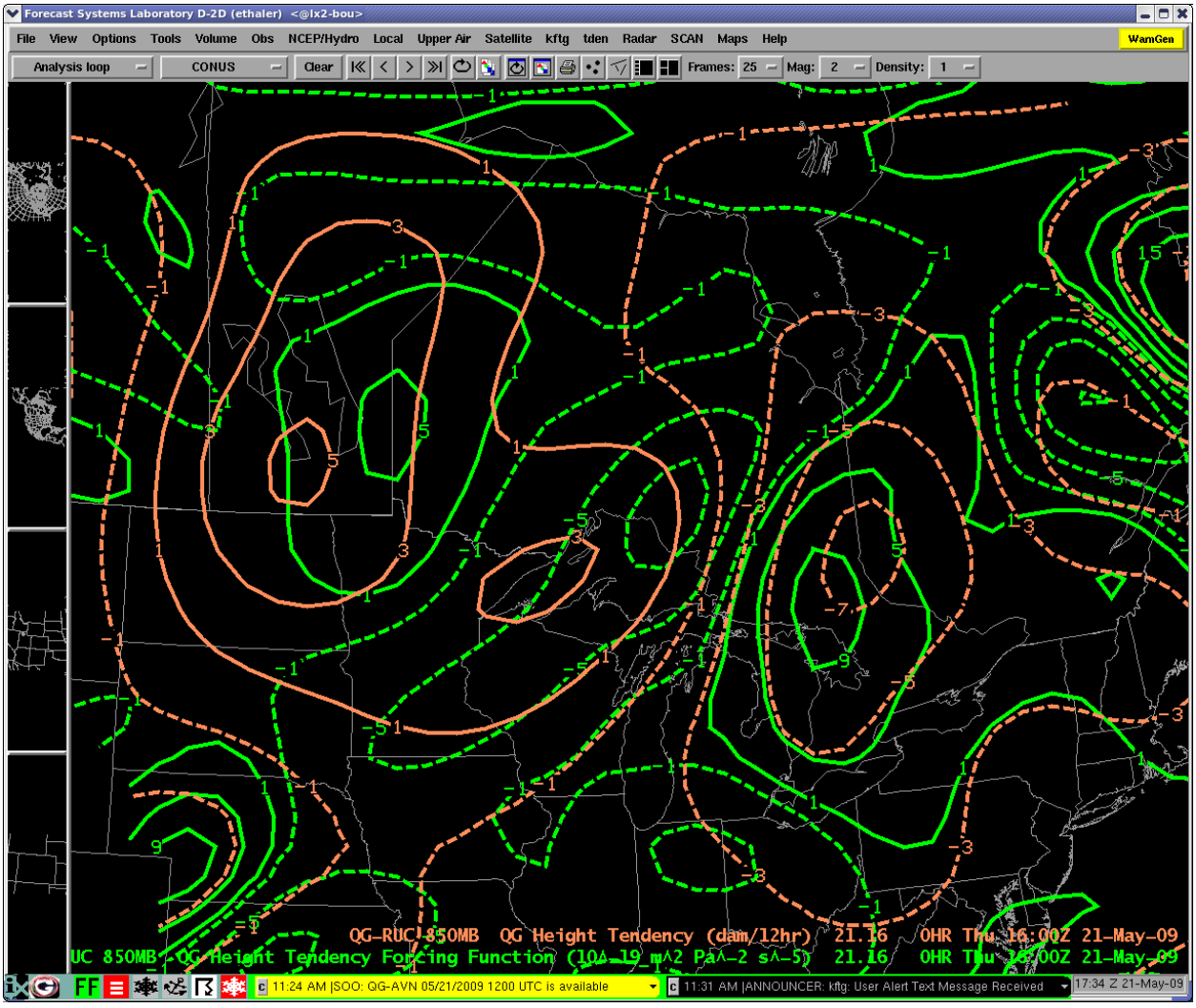

Figure 4: 850 hPa forcing function in the QG geopotential tendency equation (green, $10^{-19}\,\mathrm{m}^2\,\mathrm{Pa}^{-2}\,\mathrm{s}^{-5}$) and QG height tendency [orange, dam $(12\mathrm{hr})^{-1}$].

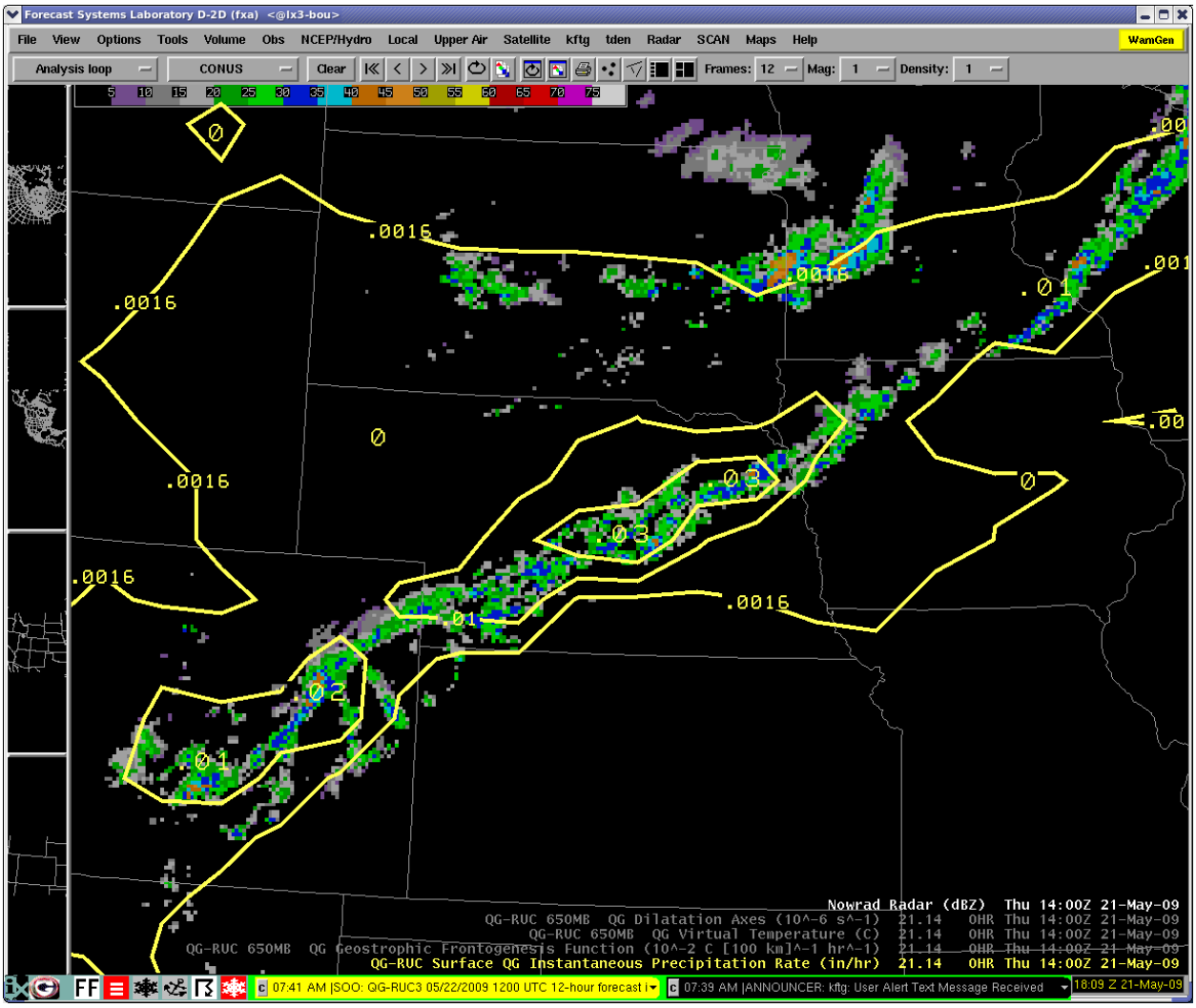

Figure 5: QG instantaneous precipitation rate (in hr^{-1}) and radar echoes (dBZ, scale at top).

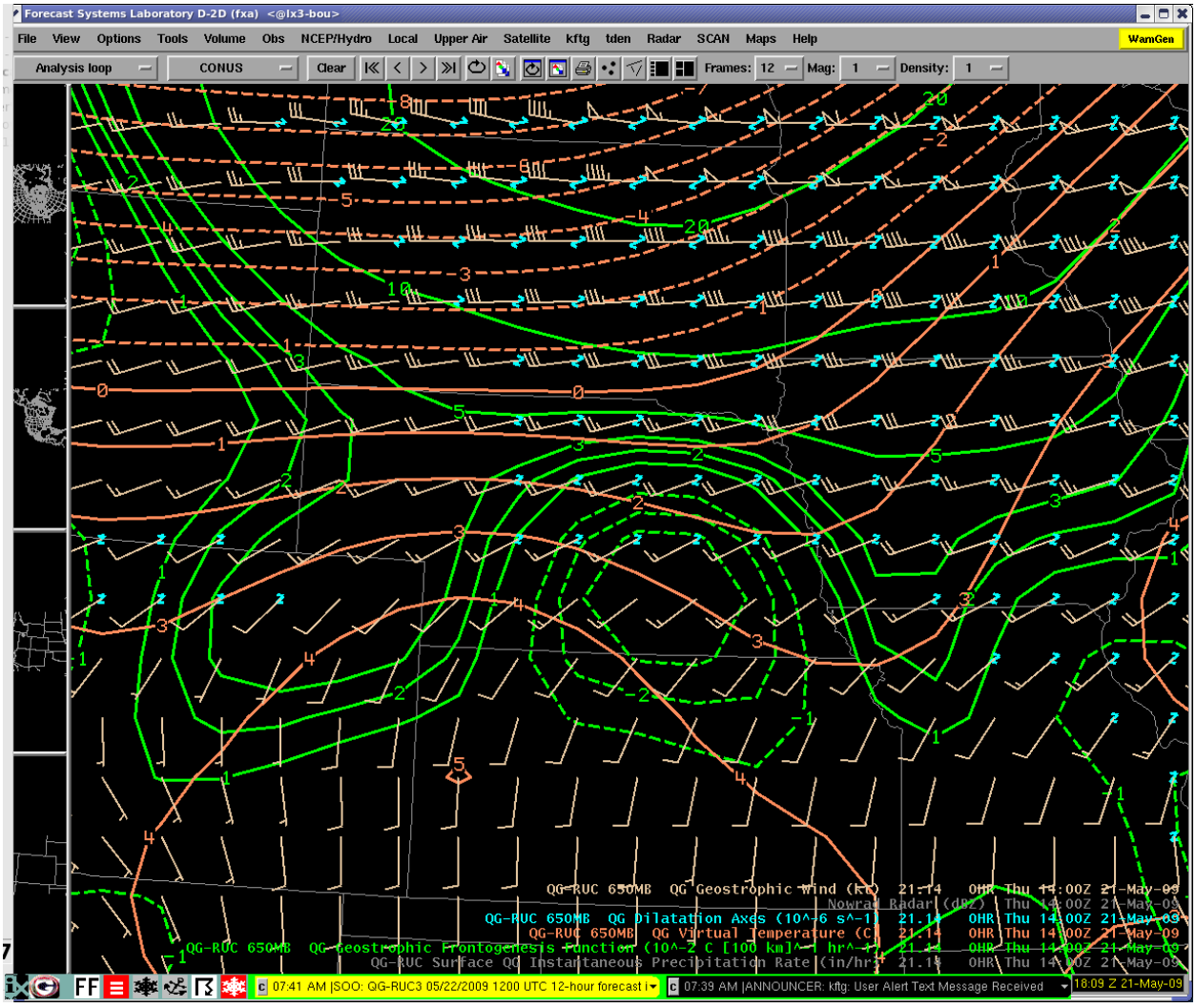

Figure 6: 650 hPa QG geostrophic frontogenesis function [green, 10^{-2} K $(100\text{km})^{-1}$ hr^{-1}], virtual temperature (orange, C), geostrophic dilatation axes (blue, 10^{-6} s^{-1}) and geostrophic wind (tan, kt).

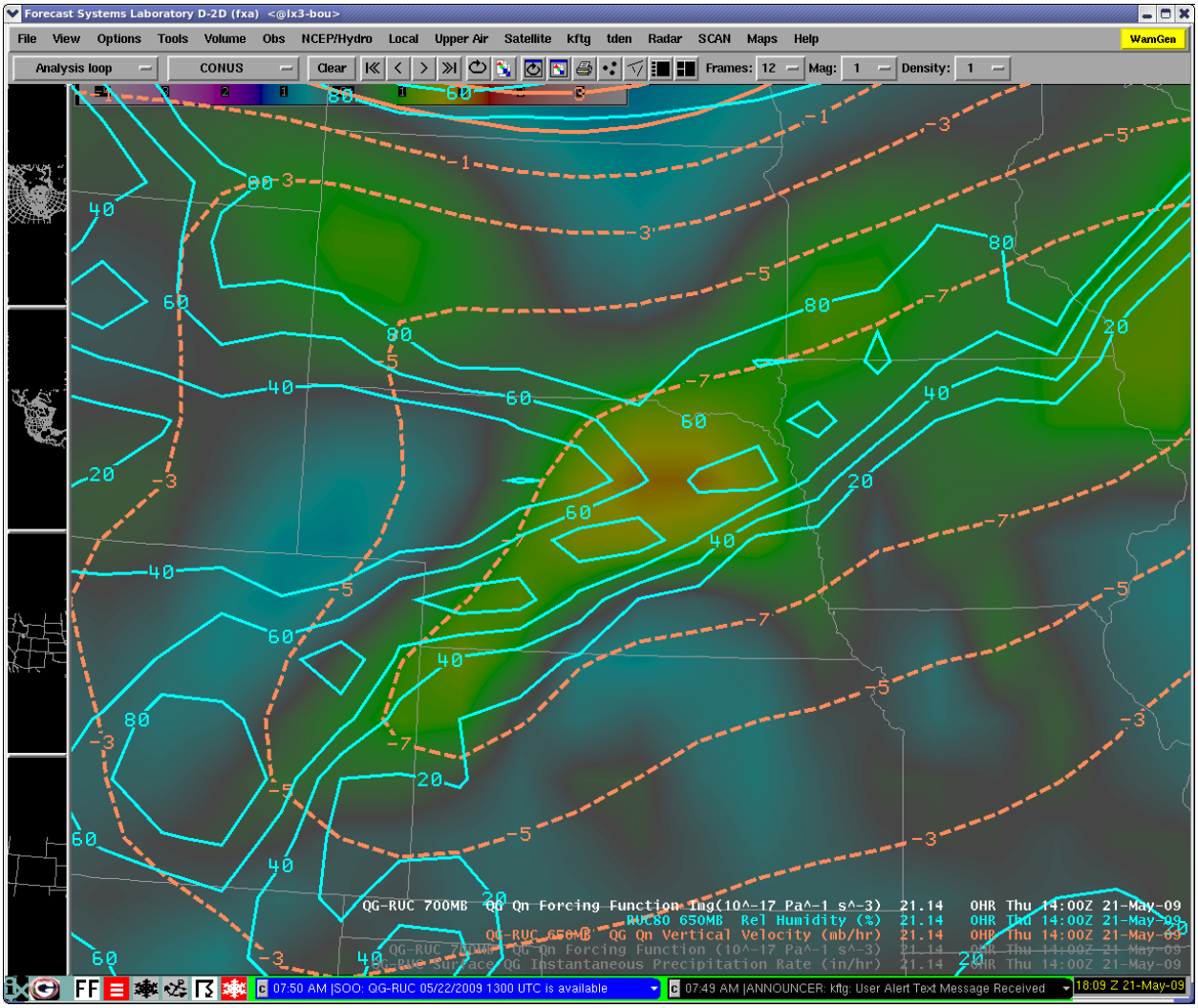

Figure 7: 700 hPa QG omega equation frontogenetical forcing function (image, 10^{-17} Pa^{-1} s^{-3}, greenish tints positive values, bluish tints negative values), relative humidity (blue, percent) and QG vertical motion response to frontogenetical forcing (orange, hPa hr^{-1}).

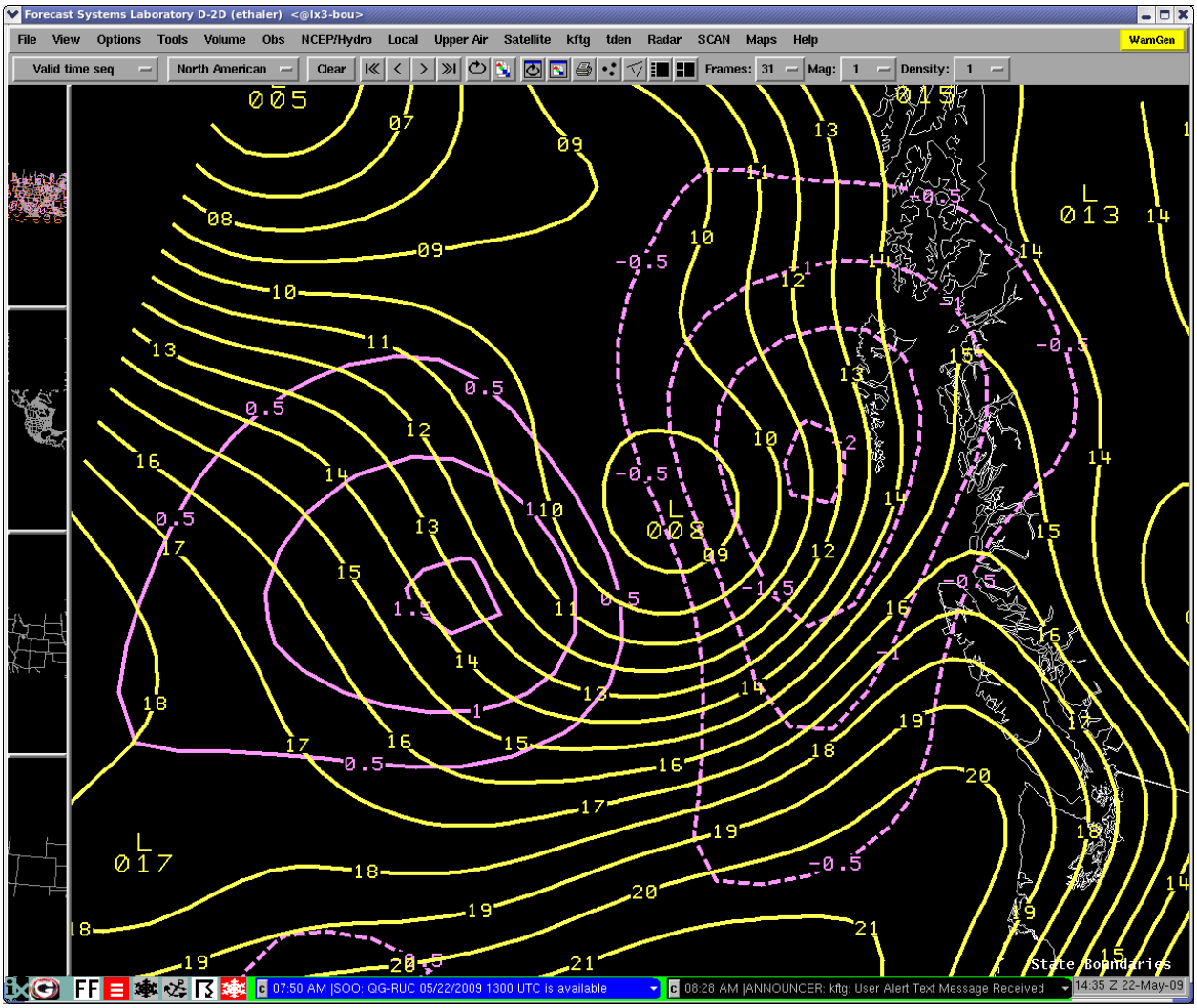

Figure 8: MSL pressure (yellow, hPa minus 1000), surface pressure tendency [purple, hPa $(3\text{hr})^{-1}$].